Optics Letters

Image reversal reactive immersion lithography improves the detection limit of focal molography

Andreas Frutiger,[1,†] Cla Duri Tschannen,[1,†] Yves Blickenstorfer,[1] Andreas M. Reichmuth,[1] Christof Fattinger,[2,3] and Janos Vörös[1,4]

[1]Laboratory of Biosensors and Bioelectronics, Institute of Biomedical Engineering, ETH Zürich, 8092 Zürich, Switzerland
[2]Roche Pharma Research and Early Development, Roche Innovation Center Basel, 4070 Basel, Switzerland
[3]e-mail: christof.fattinger@roche.com
[4]e-mail: janos.voros@biomed.ee.ethz.ch

Received 4 September 2018; revised 28 September 2018; accepted 29 September 2018; posted 1 October 2018 (Doc. ID 341991); published 26 November 2018

Focal molography is a label-free optical biosensing method that relies on a coherent pattern of binding sites for biomolecular interaction analysis. Reactive immersion lithography (RIL) is central to the patterning of molographic chips but has potential for improvements. Here, we show that applying the idea of image reversal to RIL enables the fabrication of coherent binding patterns of increased quality (i.e., higher analyte efficiency). Thereby the detection limit of focal molography in biological assays can be improved.

https://doi.org/10.1364/OL.43.005801

Label-free monitoring of biomolecular interactions is key to their understanding. Refractometric biosensors are well-established for this task in buffer but limited in complex samples [1]. Diffractometric biosensors such as focal molography (FM) are inherently robust [2]. FM is based on the scattering of coherent light by molecules bound to a coherent pattern of binding sites—termed mologram—on the surface of a thin-film optical waveguide. This coherent biomolecular assembly acts as a diffractive lens that couples a fraction of the power of the TE mode out and focuses it into an Airy disk. The intensity of this focal spot constitutes the molographic signal and is proportional to the square of the bound mass [2–4]. Since only the signal produced by coherently arranged molecules is measured, non-coherent processes such as nonspecific binding or temperature gradients are suppressed [2,4]. To obtain the necessary spatial coherence, precise patterning of binding sites with a submicrometer (150–450 nm) resolution is required. Previously, we introduced the reactive immersion lithography (RIL) process, henceforth referred to as the "standard" RIL process, as a fabrication method compatible with the requirements of focal molography [2–4]. RIL is based on interference lithography using a phase shift mask and a photoactivatable polymer adlayer. Ideally, the phase mask only diffracts into the ± 1 orders, thus producing a sinusoidal intensity distribution with half of the periodicity of the mask. Yet, due to the high refractive index immersion medium and the relatively large periods, the phase mask exhibits non-vanishing 0th and higher orders that lead to an incoherent activation of the polymer. This reduces the quality of the molographic pattern, quantified by the analyte efficiency $\eta_{[A]}$ (introduced in Ref. [4]). In short, $\eta_{[A]}$ can be thought of as the fraction of bound analyte that contributes to the molographic signal. With the standard RIL process, $\eta_{[A]}$ is limited to 0.5 for an ideal phase mask [4] and further reduced by the mentioned non-idealities. In this Letter, we present the image reversal RIL process as a way to fabricate molograms with analyte efficiencies beyond 0.5 even for a non-ideal phase mask and demonstrate that a higher analyte efficiency lowers the limit of detection in biomolecular interaction measurements.

The fabrication of molograms by the standard and the image reversal RIL process is illustrated in Fig. 1. In both cases illumination through a phase mask generates a spatially modulated dose distribution $D_I(x)$ on the coated waveguide surface. This yields a submicrometer activation distribution $\phi(x) = 1 - \exp(-bD_I(x))$, where b is the deprotection rate of the photosensitive group. The activation distribution is the blueprint of the disk-shaped coherent binding pattern (mologram). It consists of hyperbolic grating lines, with a central recess area to avoid second-order Bragg reflection (Fig. 1) [3]. Fundamental to the image reversal RIL process is that phase mask illumination is carried out at a higher average dose D_I, thereby partially saturating the activation distribution. In contrast to the standard process this is followed by passivation of the deprotected sites, whereas functionalization with a binder (biotin) specific to the target analyte (streptavidin, SAv) is only performed after an additional amplitude mask illumination step. This results in an "inverted" activation distribution $\phi_{\text{inv}}(x) = 1 - \phi(x)$.

After functionalization, both standard and "inverse" molograms exhibit a higher binding site density in some regions (ridges) compared to others (grooves). Exposure to the target analyte transduces this periodic affinity distribution into a mass distribution, which optically manifests itself as a refractive index distribution that scatters laser light of the guided mode, such that it constructively interferes in a diffraction-limited focal spot. We assume that the distributions of activation (after illumination), affinity (after functionalization), and mass (after incubation with analyte) are equivalent. Analyte mass that is present on both ridges and grooves cancels out and does not

contribute to the signal. This common mass offset is smaller for inverse mologrames (see barplots in Fig. 1).

To model mologram fabrication at different illumination doses D_I, the intensity distribution behind the phase mask must be determined [Fig. 2(a)]. For this, an exact solution to Maxwell's equations is required, which was obtained by multilayer rigorous coupled wave analysis (MRCWA) using an implementation of the framework described in Ref. [5]. The etch angle and duty-cycle of the phase mask were determined by SEM [Figs. 2(b) and 2(c)]. Due to the chirp of the mask we carried out separate simulations of an unchirped mask for each phase mask period Λ_{PM} and combined the individual intensity patterns as shown in Fig. 2. This approach is valid because adjacent periods differ only marginally. As a figure of merit for the phase mask we introduce the mask efficiency η_I, defined as the analyte efficiency when the illumination dose approaches zero [equivalent to replacing $\phi(x)$ with $D_I(x)$ in Eq. (1)]. Figure 2(d) illustrates how the mask efficiency of each period Λ_{PM} varies with distance from the mask. While over the whole mologram an oscillatory behavior can be observed due to differing Talbot lengths for each period, the average mask efficiency is largely independent of the exact distance from the phase mask.

The deprotection rate b constitutes the link between dose and activation distribution. To determine b at 405 nm, we fabricated binding spots of 300 μm on three coated Zeptochips [2] by illumination through an amplitude mask at different doses (0.5 – 10 J/cm^2), followed by functionalization according to the protocol of the standard RIL process. After incubation with 500 nM AlexaFluor555 labeled SAv (SAv^{555}), fluorescence images were acquired with the ZeptoReader (Zeptosens AG) [2]. From this, b was estimated to $(5.8 \pm 0.5) \times 10^{-4}$ cm^2/mJ [Fig. 2(e)].

The activation profiles in the sample plane were simulated using the experimentally determined value for b [Figs. 3(a) and 3(b)]. They allowed us to calculate two important quantities, $\widetilde{R}$ and $\eta_{[A]}$. The fractional receptor (binder) density $\widetilde{R}$, proportional to the gray area in Figs. 3(a) and 3(b), is the amount of binding sites on a mologram divided by the maximum binding capacity of the surface R_0 (for $\phi(x) = 1$). R_0, usually stated as a number surface density [6], depends on the surface architecture determined by the application [7]. $\widetilde{R}$ can be computed from the fractional receptor densities of the individual periods, $\widetilde{R}_i = \frac{1}{\Lambda_{PM,i}} \int_0^{\Lambda_{PM,i}} \phi_i(x)\mathrm{d}x$, via $\widetilde{R} = \sum_{N_\Lambda} w_i \widetilde{R}_i$, where N_Λ is the total number of mask periods and w_i is a weighting factor that accounts for the relative contribution of each period to the total area of a mologram. While $\widetilde{R}$ determines the maximum total surface mass density $\Gamma_{\mathrm{tot,max}}$ on a mologram, the analyte efficiency $\eta_{[A]}$ describes the fraction thereof that can actually be measured. More precisely, $\eta_{[A]}$ is defined as the ratio of equivalent coherent mass m_{coh} to the total mass m_{tot} on the mologram [4]. m_{coh} is the mass that, if placed on the center of the ridges in a δ-distributed fashion, gives rise to the same diffraction efficiency as an arbitrary mass distribution [4]. $\eta_{[A]}$ can be calculated from the relative contribution of each phase mask period $\eta_{[A]} = \sum_{N_\Lambda} w_i \widetilde{R}_i \eta_{[A],i} / \sum_{N_\Lambda} w_i \widetilde{R}_i$, where $\eta_{[A],i}$ is obtained by coherent weighting of the normalized activation profiles for each period:

$$\eta_{[A],i} = \frac{\int_0^{\Lambda_{PM,i}} \cos\left(\frac{4\pi}{\Lambda_{PM,i}} x\right) \phi_i(x)\mathrm{d}x}{\int_0^{\Lambda_{PM,i}} \phi_i(x)\mathrm{d}x}. \quad (1)$$

Coherence-weighting, Figs. 3(c) and 3(d), accounts for the relative phase of the scattered electric field from bound molecules at the focal spot. The periodicity of the cosine is motivated by

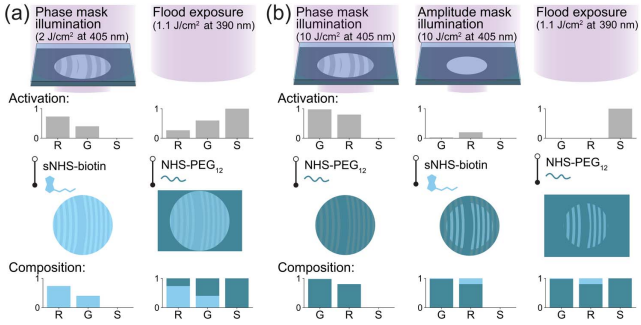

Fig. 1. Illustration of standard and image reversal RIL processes for mologram fabrication. (a) Standard process, sites that are activated upon phase mask illumination are functionalized with sNHS-biotin (light blue) [2]. Remaining photosensitive groups are deprotected by flood exposure and rendered non-binding using NHS – PEG_{12} (turquoise). The barplots depict the activation (after illumination) and the relative composition (after incubation) of ridges (R), grooves (G), and surroundings (S). (b) Image reversal is achieved by passivating the deprotected sites after phase mask illumination and using an amplitude mask to cleave the remaining photosensitive groups within a circular disk inside the holographic footprint, followed by incubation with sNHS-biotin. The last exposure serves to passivate the surroundings. While inverse mologrames have fewer specific interaction sites, their ratio of binding sites on ridges versus grooves is much larger.

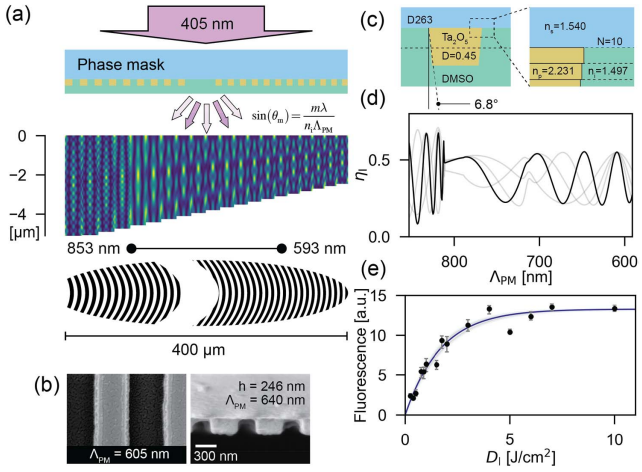

Fig. 2. (a) Numerical analysis of the intensity distribution behind the chirped phase shift mask for monochromatic TE-polarized light (405 nm). The propagating diffraction orders m (with angle θ_m) form an interference pattern, plotted for 20 mask periods from 593 to 853 nm over the corresponding Talbot length. The resulting mologram is schematically depicted with every 50th line shown. (b) Top down and side view SEM images of the cut phase mask. (c) Refractive indices and experimentally determined etch angle (6.8°) and dutycycle at mid height (0.45) used in the simulation. The profile was approximated by a 10-layer stack of rectangular profiles. (d) Mask efficiency at four different planes (1000, 1500, 2000, 3000 nm) behind the mask; one highlighted in black for better visibility. (e) The deprotection rate b of the photosensitive group at $\lambda = 405$ nm was estimated by fitting $f(D_I) = A - A\exp(-bD_I)$ to fluorescence data.

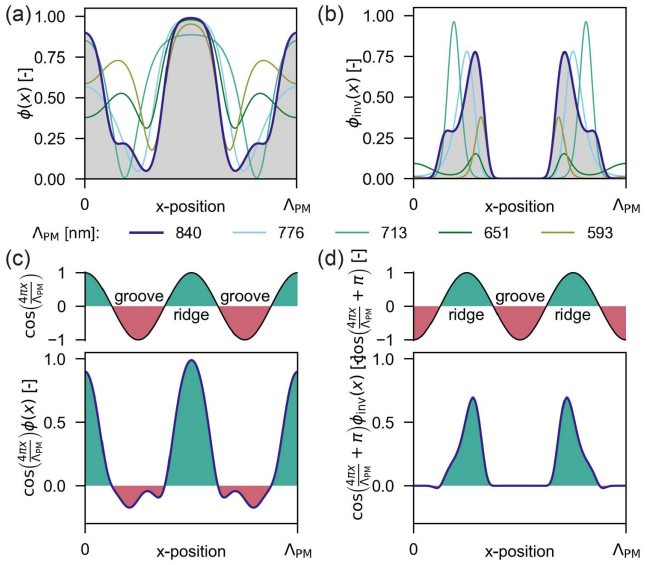

Fig. 3. (a), (b) Activation profiles for different phase mask periods Λ_{PM} at a fixed distance (2 μm) behind the mask, for (a) standard and (b) inverse mologrames fabricated at illumination doses of 2 and 10 J/cm^2, respectively. The area under the activation profiles is proportional to the fractional receptor density $\widetilde{R}$, exemplified for $\Lambda_{PM} =$ 840 nm by the shaded area. (c), (d) Coherence weighting functions: green: constructive interference (i.e., ridges), red: destructive interference (i.e., grooves). (e), (f) Coherence-weighted activation profile of (e) standard and (f) inverse mologrames, again for $\Lambda_{PM} =$ 840 nm. For inverse mologrames, the fraction of binding sites that contributes destructively to the signal is much smaller.

the fact that diffraction into the focal spot is mediated by the second overtone of the phase mask only.

To calculate the mologramic signal from $\widetilde{R}$ and $\eta_{[A]}$, we recall that it is proportional to the square of the coherent mass density $\Gamma_{coh} = \eta_{[A]}\Gamma_{tot}$ [4]. For a given Γ_{tot} (equivalently, m_{tot}), the signal is therefore larger for higher analyte efficiency mologrames. Γ_{tot} is either determined by the amount of receptors $\widetilde{R}R_0$ on the mologram, or by the total amount of analyte that binds to the sensor. Which of these is limiting depends on the assay conditions, namely the interplay of incubation time, the ratio of incubation volume to sensor size, and the affinity of the interaction [8]. Whenever the amount of analyte is limiting, mologrames with a higher $\eta_{[A]}$ will yield a larger signal in an assay. Conversely, if the analyte is abundant, then $\widetilde{R}R_0$ limits Γ_{tot}. This essentially applies when the sensor is saturated, i.e., when all available binding sites are occupied. In this case, $\Gamma_{tot} \propto \widetilde{R}$ and the mologramic signal is determined by the product $\widetilde{R}\eta_{[A]}$. Although not diagnostically relevant, this case allowed us to validate our models. By saturating the mologrames with SAv, the shape of the signal as a function of the illumination dose can be predicted from the simulated dose distribution by $I_{sig} \propto (\eta_{[A]}\widetilde{R})^2 = (\sum_{N_\Lambda} w_i \eta_{[A],i}\widetilde{R}_i)^2$. The product $\eta_{[A],i}\widetilde{R}_i$ corresponds to the area under the coherently weighted activation distribution of the period $\Lambda_{PM,i}$ [Figs. 3(e) and 3(f)]. $\Gamma_{tot} \propto \widetilde{R}$ also holds when only a fraction of the available binding sites is occupied, presupposing no depletion of analyte [6].

Experimentally, we fabricated mologrames following either the standard [2] or the image reversal RIL protocol. Chip (six fields with up to 20 mologrames each) and phase mask geometry were described in Ref. [2]; the illumination setup was introduced in Ref. [4]. After incubation with 500 nM SAv^{555} (always 500 μl for 15 min), fluorescence imaging was performed with the ZeptoReader, and Airy disk intensities were recorded either with the ZeptoReader or with the MoloReader (0.4 NA objective) [4]. Coherent mass densities were calculated from the Airy disk convoluted focal plane images and the power in the waveguide as described in Ref. [4]. All fabricated inverse mologrames had a diameter of 300 μm and an NA of 0.25 [3,4]. For direct comparison with Airy disk intensities of inverse mologrames, standard mologrames with the same specifications were used; all other standard mologrames were fabricated with a diameter of 400 μm and an NA of 0.33. All data points depict median values, and error bars delimit interquartile ranges (IQR). For fluorescence image analysis ImageJ was used, and all values were corrected for the exponential decay due to waveguide attenuation.

To confirm the effect of the illumination dose on the signal of saturated mologrames, standard mologrames (four chips) at different doses were fabricated. The Airy disk intensities (measured with the ZeptoReader) agree with the model simulated at different distances (1–6 μm) behind the phase mask [Fig. 4(a)]. Since the model only describes a proportional relationship, least squares fitting to the experimental data were used for linear scaling. The maximum signal is reached with a dose of 2.15 J/cm^2 for the presented phase mask. Notably, we were able to fabricate mologrames reproducibly without precise distance control. Our results indicate that this is due to the chirp of the phase mask. Since the Talbot length varies for each period, so does the corresponding intensity pattern. For a given period, this leads to a strong dependency of the analyte efficiency on the distance of the sample from the phase mask [Fig. 2(d)]. The mologramic signal, however, does not vary substantially with distance, but enough to explain the observed experimental variability [Fig. 4(a)].

While $\widetilde{R}$ and $\eta_{[A]}$ differ for standard and inverse mologrames fabricated at a given dose D_I, their product $\eta_{[A]}\widetilde{R}$ is equivalent (as can be shown by evaluating the corresponding equations using $\phi(x)$ and $\phi_{inv}(x)$, respectively). Therefore, the signal of saturated standard and inverse mologrames for a certain dose is the same, whereas the surface mass density Γ_{tot} required to generate the signal can vary considerably. To demonstrate this, we fabricated two chips at 10 J/cm^2, each with three fields of standard and three fields of inverse mologrames. Both mologram types gave rise to equivalent Airy disk intensities [Fig. 4(c)], while Γ_{tot} (∝ fluorescence intensity) was substantially lower for the inverse mologrames [Fig. 4(b)] (factor 9.2 measured experimentally versus 7.8 predicted from theory). This shows that inverse mologrames indeed exhibit a higher analyte efficiency.

Figures 4(d) and 4(e) show the experimental data of $\widetilde{R}$ and $\eta_{[A]}$ of standard mologrames along with the respective simulations for both standard and inverse mologrames. The data for $\widetilde{R}$ corresponds to the total surface mass density on the mologram Γ_{tot}, linearly scaled to the simulated model by least squares fitting (since $\widetilde{R} \propto \Gamma_{tot}$ under the specified conditions). Γ_{tot} for different illumination doses was calculated based on the corresponding median fluorescence intensities and the maximum SAv^{555} surface mass density $\Gamma_{tot,max}$ of 1′080 pg/mm^2 (for $\widetilde{R} = 1$), which was measured using optical waveguide lightmode spectroscopy (OWLS). The coherent mass density

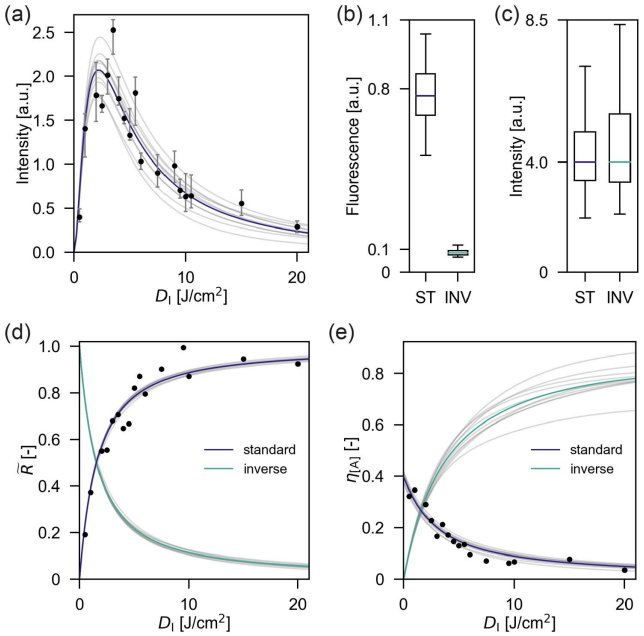

Fig. 4. (a) Airy disk intensities of standard holograms fabricated using different illumination doses. Grey: holographic signal computed from the intensity distribution at different distances (1–6 μm) behind the phase mask. Dark blue: average over these distances. (b), (c) Despite having bound appreciably less analyte, inverse holograms (INV) fabricated at 10 J/cm^2—after incubation with 500 nM SAv^{555}—give rise to equivalent Airy disk intensities compared to standard holograms (ST) fabricated at the same dose. (d) Fractional receptor density and (e) analyte efficiency as a function of illumination dose. The black dots are measurements for the standard process.

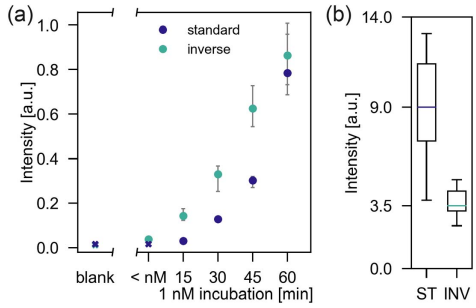

Fig. 5. (a) Image reversal RIL process increases the holographic signal at low analyte concentrations. After successive incubation steps at SAv concentrations below 1 nM, Airy disks of inverse holograms fabricated at 10 J/cm^2 were detectable, whereas for standard holograms fabricated at 2 J/cm^2 the focal spots did not stand out from the background sufficiently to be localized [×]. The blank measurements represent focal plane images arising from scattering due to waveguide roughness only. (b) Airy disk intensities of the same holograms (ST, standard; INV, inverse) after incubation with 500 nM SAv.

Γ_{coh} of the same holograms was determined from the holographic signal with the MoloReader [4], and finally $\eta_{[A]}$ was computed as $\Gamma_{coh}/\Gamma_{tot}$. The models agreed excellently with the experimental data over the entire range of illumination doses. In addition, they allowed us to predict $\widetilde{R}$ and $\eta_{[A]}$ for any phase mask and can be used to tailor the illumination dose to the application. In Ref. [4], a Γ_{coh} of 270 pg/mm^2 was determined by STED microscopy for standard holograms fabricated at 2 J/cm^2. For such holograms our models predict $\widetilde{R} = 0.57$ and $\eta_{[A]} = 0.24$. Since the chips used in Ref. [4] exhibited a $\Gamma_{tot,max}$ of 2′000 pg/mm^2, this results in a predicted coherent mass density $\Gamma_{coh} = \Gamma_{tot,max}\eta_{[A]}\widetilde{R}$ of 274 pg/mm^2. Hence, our models agree with the STED data from Ref. [4].

So far, all holograms were incubated with a concentration of analyte that effectively saturates the available binding sites $\widetilde{R}R_0$ within the incubation time of 15 min. To evaluate the signal produced by standard and inverse holograms when the amount of analyte, rather than $\widetilde{R}R_0$ is limiting, two chips were fabricated (one standard at 2 J/cm^2 and one inverse at 10 J/cm^2). Both chips were then successively incubated with 250 pM and 500 pM unlabeled SAv (15 min each). Airy disks of inverse holograms were detectable after the 500 pM incubation step [Fig. 5(a)]. Conversely, the focal spots of the standard holograms could not be localized in the speckle background arising from scattering due to waveguide roughness, indicating a coherent mass density below the limit of detection [4]. Next, both chips were subjected to four 15 min incubations with 1 nM SAv, and the Airy disk intensities were recorded after each step [Fig. 5(a)]. At these low nanomolar concentrations inverse holograms produced stronger signals, as was expected due to their higher analyte efficiency. On the other hand, after saturating both chips with 500 nM SAv, the standard holograms gave rise to 2.6-fold higher signals (higher $\widetilde{R}\eta_{[A]}$ at 2 J/cm^2 versus at 10 J/cm^2) [Fig. 5(b)], which is close to the factor 3.1 predicted from Fig. 4(a).

In summary, the presented image reversal RIL process enables the fabrication of inverse holograms, which exhibit a larger analyte efficiency compared to standard holograms and therefore require considerably less analyte to achieve a certain holographic signal. As a result, inverse holograms decrease the detection limit of focal holography whenever the number of molecules available to the sensor is limited. This is the case in most diagnostically relevant assays, which operate either under conditions where the sensor does not equilibrate on a reasonable timescale or in the mass-sensing regime (analyte depletion) [8].

[†]These authors contributed equally to this work.

REFERENCES

1. X. Fan, I. M. White, S. I. Shopova, H. Zhu, J. D. Suter, and Y. Sun, Anal. Chim. Acta **620**, 8 (2008).
2. V. Gatterdam, A. Frutiger, K.-P. Stengele, D. Heindl, T. Lübbers, J. Vörös, and C. Fattinger, Nat. Nanotechnol. **12**, 1089 (2017).
3. C. Fattinger, Phys. Rev. X **4**, 031024 (2014).
5. A. Frutiger, Y. Blickenstorfer, S. Bischof, C. Forro, M. Lauer, V. Gatterdam, C. Fattinger, and J. Vörös, "Principles for sensitive and robust biomolecular interaction analysis—the limits of detection and resolution of diffraction-limited focal holography," arxiv: 1808.07956 (2018).
5. M. G. Moharam, T. K. Gaylord, D. A. Pommet, and E. B. Grann, J. Opt. Soc. Am. A **12**, 1077 (1995).
6. T. M. Squires, R. J. Messinger, and S. R. Manalis, Nat. Biotechnol. **26**, 417 (2008).
7. E. T. Gedig, *Handbook of Surface Plasmon Resonance* (2017), Chap. 6, pp. 171–254.
8. J. W. Silzel, B. Cercek, C. Dodson, T. Tsay, and R. J. Obremski, Clin. Chem. **44**, 2036 (1998).